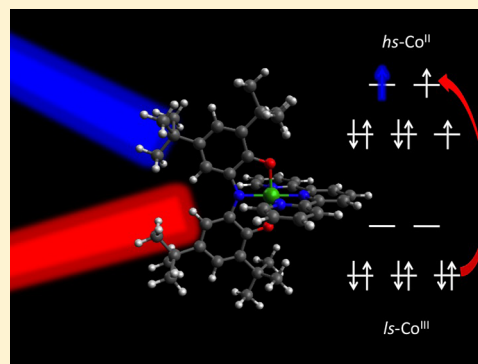


## Valence Tautomerism in Co–Dioxolene Complexes: Static and Time-Resolved Infrared Spectroscopy Study

Nicolò Azzaroli,<sup>†</sup> Andrea Lapini,<sup>†</sup> Mariangela Di Donato,<sup>†,‡</sup> Andrea Dei,<sup>‡</sup> and Roberto Righini<sup>\*,†,‡</sup><sup>†</sup>LENS, European Laboratory for Nonlinear Spectroscopy, Via Nello Carrara 1, Sesto Fiorentino, Italy<sup>‡</sup>University of Florence, Chemistry Department, Via della Lastruccia 1, Sesto Fiorentino, Italy

## Supporting Information

**ABSTRACT:** In this work, we studied the valence tautomerism process on two different Co–dioxolene complexes by means of transient infrared spectroscopy (TRIR). The molecules investigated are *ls*-Co<sup>III</sup>(Cat-N-BQ)-(Cat-N-SQ) (**DQ<sub>2</sub>**) and [*ls*-Co<sup>III</sup>(tpy)(Cat-N-SQ)]PF<sub>6</sub> (**tpy**), where Cat-NBQ = 2-(2-hydroxy-3,5-ditert-butylphenyl-imino)-4,6-ditert-butylcyclohexa-3,5-dienone, Cat-N-SQ is the dianionic radical analogue, and tpy = 2,2′-6-2″-terpyridine. DFT calculations of the harmonic frequencies for the two complexes allow us to pinpoint the normal modes to be used as markers of the semiquinonate and benzoquinonate isomers. The photoinduced one-electron charge transfer process from the radical semiquinonate ligand to the metal center leads to a *ls*-Co<sup>II</sup>(*x*)(Cat-N-BQ) electronic state (where *x* is the other ligand). Following this first step, an ultrafast ISC process ( $\tau < 200$  fs) takes place, yielding the benzoquinonate isomer (*hs*-Co<sup>II</sup>(*x*)(Cat-N-BQ)). In the experiments, we employed different excitation wavelengths on resonance with different absorption bands of the two samples. Excitation in the ligand-to-metal charge transfer (LMCT) band at  $\sim 520$  nm and in the semiquinonate band at  $\sim 1000$  nm induces the valence tautomerism (VT) in both samples. From the time evolution of the TRIR spectra, we determine the time constants of the vibrational cooling in the tautomeric state (7–14 ps) and the ground state recovery times ( $\sim 350$  ps for **tpy** and  $\sim 450$  ps for **DQ<sub>2</sub>**). In contrast, when the pump frequency is set at 712 nm, on resonance with the benzoquinonate absorption band of the second active ligand of the **DQ<sub>2</sub>**, no electron transfer takes place: the TRIR spectra basically show only ground state bleaching bands and no marker band of the tautomeric conversion shows up.

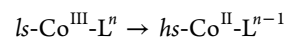


## 1. INTRODUCTION

The electron can be considered an elementary logic bit of quantum of information according to its spin. Progress in instrumental technology has provided tools allowing the detection of individual spins in dilution states. This possibility may deeply affect our view of the quantum world and induce the research to enlarge its boundaries.<sup>1</sup> However, the potential technological applications ranging from spintronics to quantum computers do not involve only the detection of the objects used but also their manipulation.<sup>2–5</sup> In the traditional investigation of bulk samples, this is easily achieved by perturbing the system with external magnetic fields, but here the problem is how to change selectively the spin state of a single molecule or of a small number of molecules. In this perspective, laser pulse based optical methods,<sup>6–8</sup> in addition to spin-polarized STM spectroscopies,<sup>9,10</sup> seem to provide the most promising tools.

Following the last consideration, it is rather obvious that the ideal magnetic systems should have magnetic properties which can be easily tuned by optical irradiation.<sup>11</sup> For this reason, systems behaving as optically switchable magnets like polycyanometallato derivatives,<sup>12–14</sup> spin crossover complexes,<sup>15–19</sup> and metal–dioxolene complexes showing redox isomerism<sup>20–28</sup> are actively investigated. Among the systems undergoing redox isomerism (valence tautomerism, VT),

cobalt–dioxolene complexes are the most attractive from the magnetic point of view. Indeed, these systems may exhibit the two important features which are believed to be the prerequisites for the observation of photoinduced optical interconversion: (i) the existence of two close in energy low-lying electronic states of different spin multiplicity and (ii) the large difference in molecular geometry of these states, mainly in the metal–donor bond length.<sup>11,18,23,27</sup> The observation that some cobalt–dioxolene derivatives exhibit photoswitchable properties can be attributed to the fulfillment of the above requirements and justify the observation of the entropy driven interconversion equilibrium:



involving an intramolecular electron transfer between a six-coordinate diamagnetic cobalt(III) metal ion (*ls*-Co<sup>III</sup>,  $t_{2g}^6$  in octahedral symmetry,  $S = 0$ ) and a coordinated dioxolene (or polyoxolene) ligand yielding a cobalt(II) adduct with oxidized

**Special Issue:** Michael D. Fayer Festschrift**Received:** May 30, 2013**Revised:** July 25, 2013

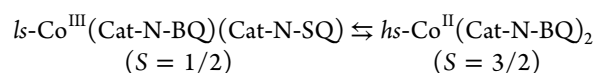
form of the same ligand ( $hs\text{-Co}^{\text{II}}$ ). Since the cobalt(II) ion has a high spin electronic configuration ( $t_{2g}^5 e_g^2$ ,  $S = 3/2$ ), a large change of magnetic properties is involved. Kinetics studies showed that nanosecond lifetimes characterize the photo-induced products at room temperature,<sup>22,29–32</sup> but these lifetimes are significantly increased to weeks and months at cryogenic temperatures.<sup>20,26,33–39</sup>

This feature justifies the technological interest toward these systems. However, there is another important point deserving consideration. These cobalt derivatives offer the possibility of using molecular systems as ideal testing grounds for the observation of sophisticated physical properties associated with the mechanism of electron transfer. Although it seems reasonable to believe that the kinetics of these processes can be largely modulated by the Franck–Condon reorganization energies and the energy differences between the ground and metastable states, the role of the electronic coupling between the  $ls\text{-Co}^{\text{III}}$  and  $hs\text{-Co}^{\text{II}}$  states is rather unclear. Indeed, the reported evidence shows that the mainstream belief that differences in spin multiplicities play a determinant role in electron transfer processes does not offer a satisfactory rationale for explaining the experimental data. It is firmly accepted that transient electronic absorption spectroscopic studies using femtosecond pulsed laser photolysis can provide important information for formulating an appropriate description of the mechanism associated to the above equilibria. In the recent past, we have shown how, by implementing the electronic absorption studies with transient infrared spectroscopy, it is possible to obtain a more significant and complete description of the process under investigation.<sup>40</sup> This consideration is particularly important if we take into account that in these complexes the electronic delocalization in the metallocycle metal–ligand bond is rather low, thus making the localized metal and ligand orbitals description an acceptable approximation.<sup>41,42</sup> Since the electron transfer process involves the increase of metal–ligand bond lengths and a change of the oxidation state of the ligand, large changes in the infrared spectra are expected. Though it should be desirable to investigate metal–ligand stretching vibrations, their location in a spectral region hardly accessible from an experimental point of view (lower than  $400\text{ cm}^{-1}$ ) precludes this opportunity. For this reason, we are limiting our analysis to the range  $1100\text{--}1700\text{ cm}^{-1}$  where most of the intraligand vibrations fall.

In this contribution, we have reconsidered a cobalt complex coordinated by the monoanion of the tridentate ligand 2-(2-hydroxy-3,5-ditert-butylphenylimino)-4,6-ditert-butylcyclohexa-3,5-dienone (Cat-N-BQ, Figure 1a) as well as by its dianionic semiquinonato radical analogue (Cat-N-SQ, Figure 1b). Though the molecule may originate four different oxidation states,<sup>43–45</sup> it is usual to find the molecule coordinated either as mononegative Cat-N-BQ or dinegative Cat-N-SQ radical. Nevertheless, it should be mentioned that, as evidenced by

Wieghardt and Chauduri,<sup>46</sup> this ligand may exhibit in some cases a more complicated behavior.

The resulting metal complex can be formulated as a mixed ligand  $\text{Co}^{\text{III}}(\text{Cat-N-BQ})(\text{Cat-N-SQ})$  derivative,  $\text{DQ}_2$ , on the basis of its structural parameters and of its magnetic and spectroscopic properties.<sup>43</sup> Indeed, the constant value of  $\chi_T = 0.4\text{ emu K mol}^{-1}$  measured in the temperature range  $4\text{--}300\text{ K}$  and the single signal at  $g = 2.00$  in its powder EPR spectrum well agree with the existence of a radical ligand coordinated to a diamagnetic  $d^6$  low-spin cobalt(III) ion. In addition, the IR and resonance Raman (RR) spectra indicate the presence of different C–O, C=O, and C=N stretching modes. This suggests that at room temperature the electron transfer process between the two coordinated ligands is slow on the vibrational time scale, thus indicating a class I character for this mixed valence compound.<sup>47,48</sup> Moreover, the temperature dependence of the spectral and magnetic properties of this compound in nonpolar solvents is indicative of the redox isomeric (valence tautomeric) equilibrium:



The critical temperature  $T_c$ , corresponding to a  $K$  value for the above equilibrium equal to 1, is close to room temperature in different organic solvents. This tautomeric equilibrium was investigated in the past in this laboratory by transient electronic absorption spectroscopy using femtosecond pulsed laser photolysis.<sup>49,50</sup> In this work, the analysis of the transient vibrational spectra of  $\text{DQ}_2$  following the electronic excitation at different visible and near-infrared wavelengths allows us to complete the picture of the photoinduced spin isomerization.<sup>32</sup> Considering that the detailed interpretation of the transient infrared spectra of  $\text{DQ}_2$  is somehow complicated by the presence of two dioxolene units with different electronic configurations, we extended our study to a simpler analogue of this metal complex, namely, to  $[\text{Co}(\text{tpy})(\text{Cat-N-SQ})]\text{PF}_6$ , **tpy**, which contains a single chelated redox active tridentate ligand and 2,2'-6,2''-terpyridine as the ancillary ligand.<sup>50</sup> The molecule contains only one dioxolene moiety (as semiquinonate); the interpretation of its behavior upon optical excitation is then free of the complication possibly affecting  $\text{DQ}_2$ . In particular, in **tpy**, it has been possible to clearly identify, with the support of *ab initio* calculations, the marker bands in the infrared spectrum to be used as diagnostic tools of the photoconversion process.

We then measured the time dependent vibrational spectra of the two complexes after photoexcitation by a subpicosecond laser pulse at wavelengths resonant with electronic transitions. The analysis of the results supports the existence of the above-mentioned redox equilibrium and provides the main kinetic parameters of the process. Our interpretation of the evolution observed in the measured transient spectra is largely based on calculations of the infrared spectra in the ground and excited states of the two compounds employing the standard DFT approach.

## 2. MATERIALS AND METHODS

**2.1. Sample Preparation.** The  $\text{Co}(\text{Cat-N-SQ})(\text{Cat-N-BQ})$  ( $\text{DQ}_2$ ) and  $[\text{Co}(\text{tpy})(\text{Cat-N-SQ})]\text{PF}_6$  (**tpy**) complexes were prepared according to previously reported procedures.<sup>44,50</sup>

**2.2. Experimental Setup.** **2.2.1. Electronic Absorption and FT-IR.** All UV–vis absorption spectra were recorded with a Lambda 950 Perkin-Elmer spectrophotometer; Bruker Alpha-T

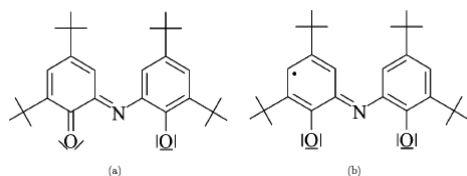


**Figure 1.** (a) Cat-N-BQ dioxolene ligand; (b) (Cat-N-SQ) dioxolene ligand.

and Shimadzu FTIR-8400S spectrometers were used for measuring the mid-infrared spectra.

**2.2.2. Time Resolved Infrared Spectroscopy.** Time resolved infrared (TRIR) experiments are performed using the UV pump mid-IR probe setup previously described.<sup>40,51,52</sup> Briefly, about 20% of the output of a regenerative amplified Ti:sapphire oscillator system (Coherent Legend Elite, 810 nm central wavelength, 1 kHz rep. rate, >3 mJ per pulse, 35 fs pulse duration) is employed for the experiment. A fraction ( $\sim 350 \mu\text{J}$  per pulse) of the output is delivered to a TOPAS (Light Conversion) Optical Parametric Amplifier (OPA), producing tunable NIR pulses. The output is converted, by means of a  $300 \mu\text{m}$  thick BBO crystal, to visible pulses to be used for exciting the electronic transitions. A second fraction ( $\sim 300 \mu\text{J}$  per pulse) of the 810 nm fundamental is used to pump a home-built OPA; difference frequency of idler and signal is finally generated in 1 mm thick AgGaS<sub>2</sub> crystal. Around  $\lambda = 6 \mu\text{m}$ , spectrally broad pulses (typical bandwidth  $>200 \text{ cm}^{-1}$ ) are obtained with energy of about  $1 \mu\text{J}$  and duration of  $\sim 150 \text{ fs}$ . The probe and reference beams, of equal intensity, are obtained by reflection from the faces of a wedged CaF<sub>2</sub> plate and focused into the sample by a parabolic mirror. Both beams are sent to a flat-field monochromator and imaged into a double 32-channel array mercury cadmium telluride (MCT) infrared detector.<sup>40</sup>

**2.3. Ab Initio Calculations.** All the quantum chemical calculations were performed by the DFT<sup>53</sup> method implemented in Gaussian 09<sup>54</sup> with the UB3-LYP hybrid exchange and correlation functional.<sup>55</sup> In most cases, we used 6-31G\*\* as the basis set; on some occasions, this was joined to STO3-G. With this protocol, we calculated the electronic ground and tautomeric states, paying attention to two main parameters. The first is the spin density of the molecular fragments: the Co atom and the ligands. In the ground state, we expect only one unpaired electron completely localized on one active ligand in accomplishment with the low-spin Co<sup>III</sup> electronic configuration of the metal center and of the radical semiquinonate configuration for the active ligand. The second parameter considered is the bond distance between Co and ligand atoms. The crystallographic data reported in the literature for low-spin Co<sup>III</sup> and high-spin Co<sup>II</sup> complexes show an increment of the Co–L distance from  $\sim 1.88$  to  $\sim 2.10 \text{ \AA}$  as a consequence of the spin transition from  $ls\text{-Co}^{\text{III}} d^6 (t_{2g})^6(e_g)^0$  to  $hs\text{-Co}^{\text{II}} d^7 (t_{2g})^5(e_g)^2$  that populates the antibonding  $e_g$  molecular orbitals.<sup>50,56</sup> The FT-IR spectra calculated for both species allow us to pinpoint the spectral features to be taken as a diagnostic of the spin transition in the experimental TRIR spectra.

**2.4. Data Analysis.** For the quantitative analysis of TRIR data, we used a combined approach, consisting of singular values decomposition and global fitting analysis. Both steps are performed using the GLOTARAN package.<sup>57</sup> The protocol adopted is fully described in a previous work.<sup>40</sup> Briefly, to avoid spectral artifact due to perturbed free induction decay and to cross-phase modulation effects, we excluded from our analysis the spectra recorded at delay times shorter than 500 fs.<sup>58–62</sup> First, we obtained the components number by singular values decomposition (SVD); then, by means of a global fitting procedure, we analyzed the whole ensemble of kinetic data. The combination of global analysis and SVD provides a good control of the components number used in the fitting.<sup>57,63</sup> The goal of global analysis is to decompose the whole data matrix into time-independent spectra and wavelength-independent kinetics traces.<sup>64</sup> Once the number of components has been

defined, the very next step involves the parametrization of the time evolution of the relative intensities of the associated spectral contributions (evolution associated spectra, EAS).

### 3. RESULTS

**3.1. FT-IR Spectra and Normal Mode Assignment.** The infrared spectra of **tpy** and of **DQ<sub>2</sub>** were recorded in deuterated dichloromethane (CD<sub>2</sub>Cl<sub>2</sub>) and tetrachloromethane (CCl<sub>4</sub>) solution, respectively (Figure 2). We focus our investigation on

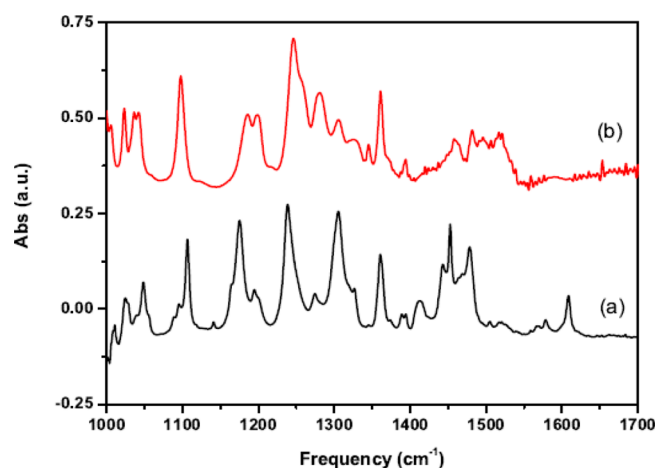


**Figure 2.** Infrared spectra in the  $1000\text{--}1700 \text{ cm}^{-1}$  region: (a) experimental FT-IR spectrum in CD<sub>2</sub>Cl<sub>2</sub> of the **tpy** complex; (b) experimental FT-IR spectrum in CCl<sub>4</sub> of the **DQ<sub>2</sub>** complex.

the region between  $1100$  and  $1700 \text{ cm}^{-1}$ ; in fact, at higher frequencies, the spectrum mainly consists of aliphatic and aromatic C–H stretching modes which are not informative on the VT transformation, while at lower frequency a large part of the spectrum is not accessible due to the absorption of the solvent. The DFT calculations give the basis for the spectral assignment.

Selected observed and computed frequencies of **tpy** complex are reported in Table 1. The calculated spectrum is in excellent

**Table 1. Characteristic Vibrational Frequencies for [Co<sup>III</sup>(tpy)(Cat-N-SQ)]PF<sub>6</sub>**

Exp. (cm <sup>-1</sup> )	UB3-LYP (cm <sup>-1</sup> )	approx. description
1104	1101	$\delta(\text{C—H})$ , breathing
1173, 1192	1178, 1191	$\delta(\text{C—H})$ , $\delta(\text{C—C})$ (t-bu), breathing
1238	1232	$\nu(\text{C—C})$ , $\delta(\text{C—C})$ (t-bu)
1274	1268	$\delta(\text{C—H})$ (sp <sup>2</sup> ), $\nu(\text{C—C})$
1304	1302	$\nu(\text{C=C})$ , $\nu(\text{C—C})$ , $\nu(\text{C=O})$
1411	1409	$\nu(\text{C=C})$ , $\delta(\text{C—H})$
1451	1443	$\nu(\text{C=C})$ , $\delta(\text{C—H})$
1579–1607	1576–1609	$\nu(\text{C=C})$ , $\delta(\text{C—H})$ , $\nu(\text{C=N})$ tpy

agreement with the experimental one, not only for the vibrational frequencies but also for the relative intensities. In the first two columns, the experimental and calculated frequencies are compared; the third column gives an approximate description of the corresponding normal modes, as they result from the calculations. All resonances from  $1100$  up to  $1500 \text{ cm}^{-1}$  are mainly due to vibrations of the active ligand, as the vibrational modes of the ancillary ligand (tpy) are concentrated at higher frequencies ( $1570\text{--}1600 \text{ cm}^{-1}$ ).



The first band at  $1104\text{ cm}^{-1}$  of spectrum a corresponds to active ligand's C—H bending, with relevant contribution of ring breathing. Very similar is the mode structure of the doublet at  $1173$  and  $1192\text{ cm}^{-1}$ , with some additional contribution of the isobutyl group C—C bending. The band at  $1238\text{ cm}^{-1}$  corresponds to the combination of the ligand's C—C bending and stretching, while the very low intensity band at  $1274\text{ cm}^{-1}$  is due to C—C stretching and aromatic C—H bending. The most important band is centered at  $1304\text{ cm}^{-1}$  and involves C=O, C—C, and C=C stretching. Its diagnostic role will be made evident in the next section by the comparison with the calculated spectrum of the  $[hs\text{-CoII}(\text{tpy})(\text{Cat-N-BQ})]\text{PF}_6$  tautomeric form. Other bands at  $1411$  and  $1451\text{ cm}^{-1}$  are due to the combinations of C=C stretching and C—H bending vibrations. As mentioned above, the vibrations of the ancillary ligand are concentrated in the region between  $1579$  and  $1609\text{ cm}^{-1}$ .

Equally satisfactory is the agreement of the calculated and experimental frequencies of  $\text{DQ}_2$ . Table 2 shows the

**Table 2. Characteristic Vibrational Frequencies for  $\text{Co}^{\text{III}}$  (Cat-N-BQ)(Cat-N-SQ)**

Exp. ( $\text{cm}^{-1}$ )	UB3-LYP ( $\text{cm}^{-1}$ )	approx. description
1098	1094	$\delta(\text{C—H})$ , breathing
1183, 1197	1177, 1189	$\delta(\text{C—H})$ , $\delta(\text{C—C})$ (t-bu)
1246	1255	$\nu(\text{C—C})$ , $\delta(\text{C—C})$ (t-bu)
1279	1274	$\delta(\text{C—H})$ ( $\text{sp}^2$ ), $\nu(\text{C—C})$
1327	1311	$\nu(\text{C=C})$ , $\nu(\text{C—C})$ , $\nu(\text{C=O})$
1450	1443	$\nu(\text{C=C})$ , $\delta(\text{C—H})$
1520	1522	$\nu(\text{C=C})$ , $\delta(\text{C—H})$

comparison of experimental and calculated IR frequencies for the  $\text{DQ}_2$  complex. The experimental data are recorded in  $\text{CCl}_4$  solution, while the calculated ones are obtained with the same computational protocol adopted for **tpy**. Noteworthy, the frequencies and the approximate description of the vibrational modes considered are very similar.

**3.2. Electronic Absorption Spectra.** The electronic spectra of **tpy** dissolved in  $\text{CH}_2\text{Cl}_2$  (a) and of  $\text{DQ}_2$  dissolved in  $\text{CCl}_4$  (b) are presented in Figure 3.

The electronic spectra of **tpy** and  $\text{DQ}_2$  at  $\lambda > 600\text{ nm}$  show remarkable differences. Only two absorption peaks are observed for **tpy** at  $937$  and  $1063\text{ nm}$ , and are assigned to transitions of

the dioxolene ligand, which is present in its semiquinonate electronic configuration. The spectrum of  $\text{DQ}_2$  instead has four peaks at  $704$ ,  $807$ ,  $899$ , and  $1045\text{ nm}$ . We recall that the two dioxolene ligands of  $\text{DQ}_2$  are present in two different oxidation states: semiquinonate (Cat-N-SQ) and benzoquinonate (Cat-N-BQ). In analogy with the **tpy** spectrum, we assign the  $899$ – $1045\text{ nm}$  doublet to the semiquinonate moiety, while the two peaks at  $704$  and  $807$  are attributed to the benzoquinonate ligand. Following the assignment of Gentili et al.,<sup>32</sup> we identify the band at  $526\text{ nm}$  in Figure 3b as the ligand-to-metal charge transfer (LMCT) transition of  $\text{DQ}_2$ ; the same transition in **tpy** corresponds to the sharp band at  $521\text{ nm}$  (Figure 3a).

The arrows in Figure 3 indicate the different excitation wavelengths used in our experiments. By setting the excitation pulse at  $\lambda = 521\text{ nm}$  for **tpy** and at  $\lambda = 525\text{ nm}$  for  $\text{DQ}_2$ , the charge transfer transition is directly induced. Excitation is performed at the other indicated wavelengths in order to verify if, by populating different electronic states, the VT conversion can be achieved.

For the purpose of clarity, in the following sections, the results obtained for **tpy** and  $\text{DQ}_2$  are described and discussed separately.

**3.3.  $[\text{Co}(\text{tpy})(\text{Cat-N-SQ})]\text{PF}_6$ .** 3.3.1. *Ab Initio Calculations.* We used the spin densities as a parameter to verify that the correct electronic configurations are calculated. The results obtained for the  $ls\text{-Co}^{\text{III}}$  are summarized in Table 3, showing

**Table 3. Spin Densities Calculated on Different Fragments of Molecule for  $ls\text{-Co}^{\text{III}}$**

fragment	spin density
Co(III)	−0.00129
tpy	0.00730
Cat-N-SQ	0.99399
total	1.00

the existence of only one unpaired electron totally localized on the active ligand, in agreement with the  $d^6$  low spin configuration of the metal center and the radical nature of the active ligand, with total spin  $S = 1/2$ . As a cross-check, in Table 4, we compare the calculated Co–L bond distances with the crystallographic data from the literature.<sup>44,50</sup> The good correspondence of these data confirms the reliability of the

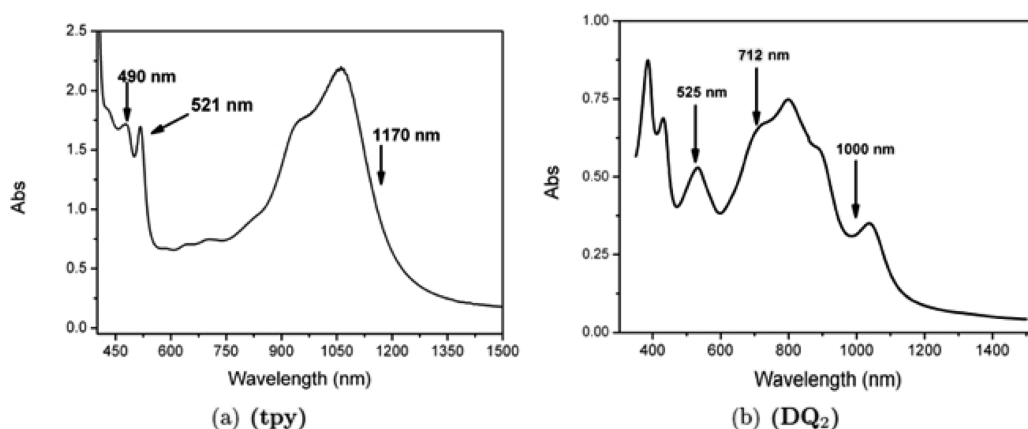


**Figure 3.** Electronic absorption spectra of (a) **tpy** dissolved in  $\text{CH}_2\text{Cl}_2$  and of (b)  $\text{DQ}_2$  dissolved in  $\text{CCl}_4$ . The arrows indicate the excitation wavelengths of TRIR experiments.

**Table 4.** Comparison of Calculated Co–L Bond Distances with Literature Data<sup>50</sup> for *ls*-Co<sup>III</sup>

M–L distances (Å)			
calculated (this work)		from ref 50	
Co–N1(tpy)	1.88	Co–N1(tpy)	1.88
Co–N2(tpy)	1.96	Co–N2(tpy)	1.91
Co–N3(tpy)	1.96	Co–N3(tpy)	1.92
Co–N(SQ)	1.87	Co–N(SQ)	1.83
Co–O1(SQ)	1.88	Co–O1(SQ)	1.88
Co–O2(SQ)	1.88	Co–O2(SQ)	1.88

calculated electronic states. For the calculations of the *hs*-Co<sup>II</sup> tautomeric form, we took into account the same parameters. The spin densities of the molecular fragments and the Co–L bond distances are reported in Tables 5 and 6, respectively.

**Table 5.** Spin Densities Calculated on Different Fragments of Molecule for *hs*-Co<sup>II</sup>

fragment	spin densities
Co(II)	2.772707
tpy	0.093722
Cat-N-BQ	0.133574
total	3.00

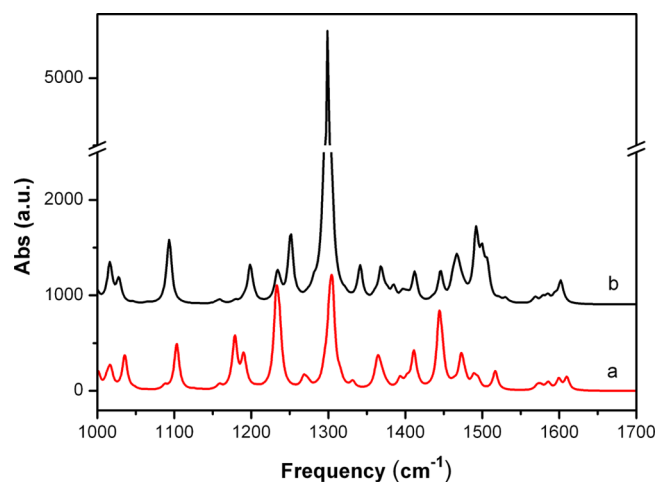
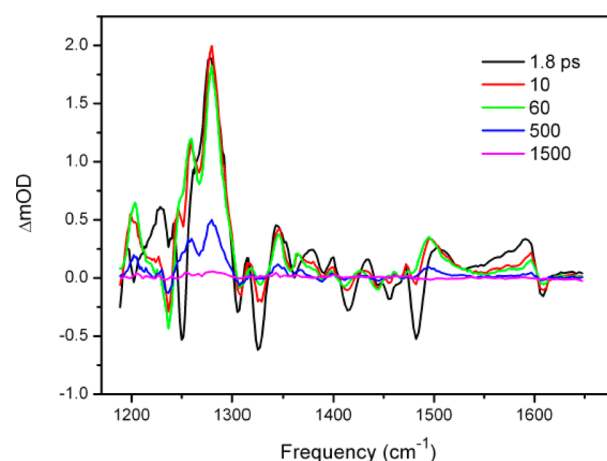
**Table 6.** Comparison of M–L Bond Distances Calculated for *hs*-Co<sup>II</sup> and [*hs*-Ni<sup>II</sup>(Cat-N-BQ)<sub>2</sub>]<sup>45</sup>

Co–L distances (Å) (this work)		Ni–L distances (Å) from ref 45	
Co–N1(tpy)	2.17	Ni–N1	2.02
Co–N2(tpy)	2.17	Ni–N2	2.02
Co–N3(tpy)	2.05	Ni–O1	2.04
Co–N(BQ)	2.06	Ni–O2	2.03
Co–O1(BQ)	2.03	Ni–O3	2.02
Co–O2(BQ)	2.03	Ni–O4	2.02

According to Table 5, three unpaired electrons are localized on the metal center, in accomplishment with the d<sup>7</sup> high spin configuration of Co; no unpaired electron is present on the active ligand. To verify the computed bond distances of the benzoquinonate isomer, we compare them with crystallographic data from the literature of the *hs*-Ni<sup>II</sup>(Cat-N-BQ)<sub>2</sub>;<sup>45</sup> see Table 6.

The comparison of the calculated IR spectra of the two conformers, shown in Figure 4, allows one to identify the spectral features to be used as diagnostic tools of the tautomeric interconversion. From Figure 4, we identify two important pieces of evidence, consisting of intensity enhancement of two bands of the *hs*-Co<sup>II</sup> tautomer involving  $\nu(\text{C}=\text{O})$  and  $\nu(\text{C}=\text{C})$  vibrations. The first one at  $\sim 1300\text{ cm}^{-1}$  is very evident; less pronounced, but still well visible, is the intensity increase of the band at  $1490\text{ cm}^{-1}$ . These are the spectral regions to be primarily checked in the experimental TRIR spectra.

**3.3.2. TRIR.** In Figure 5, we present transient infrared spectra recorded at different delay times following excitation at 490 nm. A prominent peak centered at  $1280\text{ cm}^{-1}$  is observed; its intensity starts to decrease after  $\sim 60\text{ ps}$ . A rather complex structure is observed on the low frequency side of this band. The weak shoulder visible at 1.8 ps delay becomes a well-defined peak centered at  $1258\text{ cm}^{-1}$ , which grows in intensity up to 60 ps. At lower frequencies, we notice the absorption

**Figure 4.** Calculated FTIR spectra of tpy for (a) *ls*-Co<sup>III</sup> configuration and (b) *hs*-Co<sup>II</sup> configuration.**Figure 5.** tpy TRIR spectra recorded after excitation at 490 nm. Delay times are given in the legend.

centered at  $1228\text{ cm}^{-1}$ , whose evolution is very fast: after 10 ps, it has practically disappeared. In the high frequency region, there are two main transient signals, at  $1494$  and  $1590\text{ cm}^{-1}$ : the highest in energy is attributed to vibrational modes of the ancillary ligand (tpy). The other has the negative band centered at  $1480\text{ cm}^{-1}$  and the absorption positive band at  $1495\text{ cm}^{-1}$ ; it is assigned to the  $(\nu(\text{C}=\text{C}) + \nu(\text{C}=\text{O}))$  mixed mode.

The TRIR spectra obtained by exciting the sample at 521 and 1170 nm are shown in Figure 6a and b, respectively. They are very similar to those in Figure 5; in particular, we focus our attention on the two bands centered at  $1280$  and  $1495\text{ cm}^{-1}$ . In the spectra of Figure 6a, the band at  $1280\text{ cm}^{-1}$  shows the same evolution described above for the bands in Figure 5. Figure 6b evidences some little differences. The dynamics of the low frequency shoulder of the  $1280\text{ cm}^{-1}$  band is faster in comparison to the behavior observed after excitation at 521 and 490 nm. In fact, it appears as a well-defined peak already at 1.8 ps, while in the other two experiments it reaches its final shape in about 60 ps. We can notice also some differences in the relative intensities of the bands of the three spectra.

**3.4. Co(Cat-N-SQ)(Cat-N-BQ).** **3.4.1. Ab Initio Calculations.** We adopted the same calculation protocol already described for the tpy complex. Also for DQ<sub>2</sub>, the calculated spin densities and Co–L distances are in good agreement with the

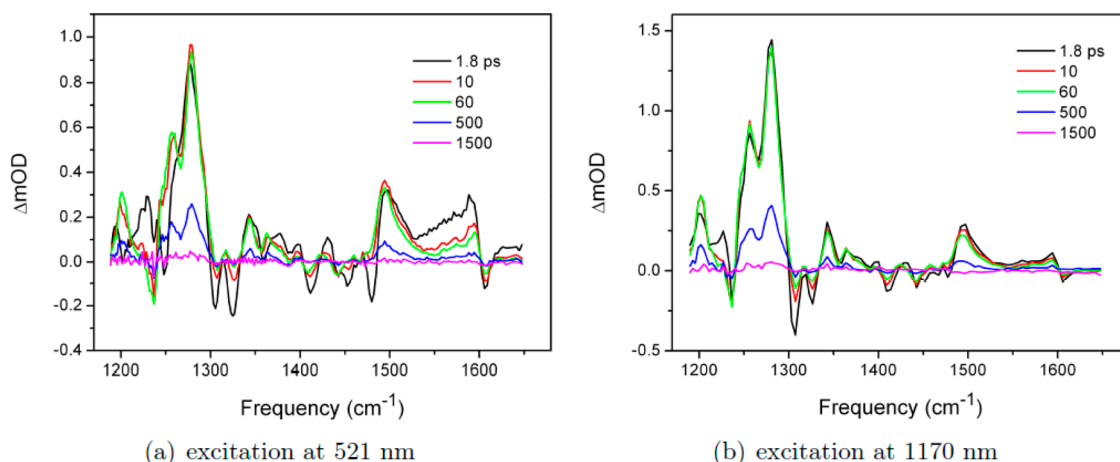


**Figure 6.** TRIR spectra of **tpy** excited at 521 and 1170 nm. Delay times are given in the legend.

reported data (see the Supporting Information). In Figure 7, we present the comparison between the calculated infrared spectra

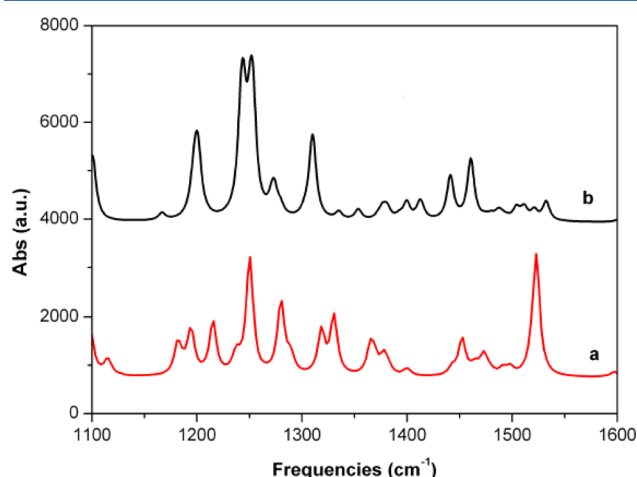


**Figure 7.** Calculated FTIR spectra of **DQ<sub>2</sub>** for (a) *ls*-Co<sup>III</sup> configuration and (b) *hs*-Co<sup>II</sup> configuration.

of **DQ<sub>2</sub>** in the *ls*-Co<sup>III</sup> (a) and *hs*-Co<sup>II</sup> (b) tautomeric forms. The most evident spectral change resulting from Figure 7 concerns the (C—C) stretching band at ~1250 cm<sup>−1</sup>; the

single peak in part a becomes a doublet in part b, with some increase in intensity too. A large decrease in intensity of the peak at ~1525 cm<sup>−1</sup>, assigned to the (C=C) stretching and (C—H) bending, is also observed on going from *ls*-Co<sup>III</sup> to *hs*-Co<sup>II</sup>. However, we have to notice that, while the agreement of the calculated and experimental frequencies of the *ls*-Co<sup>III</sup> form of **DQ<sub>2</sub>** is very good, some discrepancies can be observed for the intensities, in particular in the high frequency region (1400–1600 cm<sup>−1</sup>). This suggests we should focus our search for diagnostic evidence of the tautomeric conversion to the 1200–1300 cm<sup>−1</sup> region of the TRIR spectra.

Excitation at 525 and 1000 nm yields very similar TRIR spectra, as shown in Figure 8a and b. The intense absorption band centered at 1233 cm<sup>−1</sup> is present only at early times (black line spectra in Figure 8, corresponding to 1.8 ps delay); its dynamics is very fast, and after 30 ps, it has disappeared.

At short delay time, the strongest absorption band consists of two peaks centered at 1276 and 1295 cm<sup>−1</sup>, as expected according to the calculation (Figure 7). Similarly to what was observed for **tpy**, as the delay time increases, this absorption band reveals a more complex structure on its low frequency side, developing a third peak at 1258 cm<sup>−1</sup>. In the high frequency region, we observe an absorption band centered at 1490 cm<sup>−1</sup> and two bleaching bands at 1458 and 1518 cm<sup>−1</sup>.

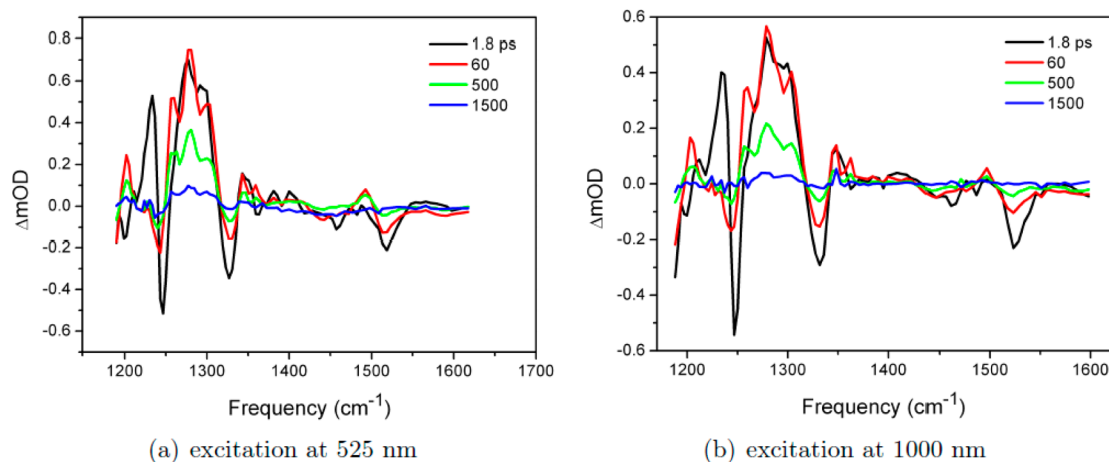


**Figure 8.** TRIR spectra of **DQ<sub>2</sub>**: (a) excitation at 525 nm; (b) excitation at 1000 nm.

A completely different transient spectrum (Figure 9) is obtained by exciting the sample at 712 nm. The region between

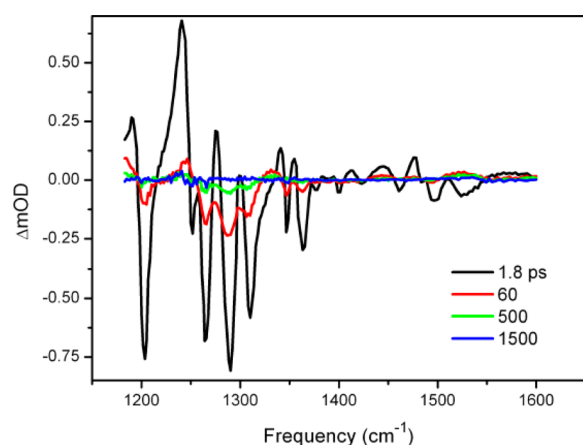


Figure 9. TRIR spectra of  $DQ_2$  with excitation at 712 nm.

1300 and 1600  $\text{cm}^{-1}$  is completely different from the other measurements; in particular, the bands around 1300 and 1500  $\text{cm}^{-1}$  are not present. Except for the spectrum at 1.8 ps delay, only bleaching bands are present, whose amplitude decreases in the time scale of hundreds of picoseconds.

## 4. DISCUSSION

**4.1.  $[\text{Co}(\text{tpy})(\text{Cat-N-SQ})]\text{PF}_6$ .** The first indication coming from the analysis of the TRIR experiments performed on **tpy** is that, whatever the excitation wavelength employed, the same electronic state is populated after a delay time of very few tens of picoseconds. To validate this conclusion, we performed a global analysis of the TRIR data adopting a two-compartment sequential kinetic model: the results are shown in Table 7, and the corresponding EAS (evolution associated spectra) are presented in Figure 10.

The very similar values of the slower time constants  $\tau_2$  reported in Table 7 confirm that in all the cases the same electronic state is populated in less than 30 ps. The values of  $\tau_1$  are similar for excitation at 490 and 521 nm, while this time constant is almost twice shorter when 1170 nm pulses are used. Figure 11 shows a detail of the main absorption band at 1278  $\text{cm}^{-1}$  from Figures 5 and 6. A blue shift with increasing delay time is clearly observed after excitation at 490 and 521 nm; the same effect is not observed when the sample is excited at 1170 nm. Our interpretation is that the  $t_1$  time constant reflects vibrational cooling in the final state. This effect is well visible when large excess energy is deposited in the molecule; excitation at 1170 nm instead populates the same state in a lower vibrational level, thus making the effect of vibrational cooling much less evident. This idea is supported by the previous study of Gentili et al.<sup>32</sup> their transient absorption spectroscopy (TAS) measurements on the  $DQ_2$  complex did not reveal any dynamics with time constants in the range of  $\tau_1$ . On the basis of our TRIR measurements, of the quantum

calculations and of previous results present in the literature concerning time-resolved experiment on Co–dioxolene complexes,<sup>32,40</sup> we can propose for the electronic excited state evolution the four-step process graphically synthesized in Figure 12. The first step is the electronic excitation: a ligand-to-metal one electron transfer takes place with the pump wavelength set at 490 and 521 nm, populating the  $ls\text{-Co}^{\text{II}}(\text{tpy})(\text{Cat-N-BQ})$  state. Excitation at 1170 nm promotes an active ligand's internal transition ( $n \rightarrow \pi^*$  or  $\pi \rightarrow \pi^*$ ). The second step consists of an intersystem crossing (ISC) process, which populates the  $hs\text{-Co}^{\text{II}}(\text{tpy})(\text{Cat-N-BQ})$  electronic tautomeric state. Its time scale is very fast, definitely below our time resolution ( $\sim 200$  fs): whatever the excitation wavelength employed, we cannot reveal this very fast process. However, the similarity of the transient IR spectra measured for all the excitation wavelengths indicates that this process transfers population to the same electronic state.

As we noticed in section 3.3.1, our ground and excited state quantum calculations point out two regions of the vibrational spectrum that can be used as diagnostic tools of the tautomeric conversion. The main evidence for valence tautomerization comes from the appearance of the most intense absorption band at  $\sim 1300$   $\text{cm}^{-1}$ , and a second indication comes from the absorption band at  $\sim 1500$   $\text{cm}^{-1}$  in the TRIR spectra. The third step is the previously discussed process of vibrational cooling toward the bottom of the metastable high-spin electronic state. The fourth and final step is the ground state recovery, yielding the stable low-spin  $\text{Co}^{\text{III}}$  state.

**4.2.  $\text{Co}(\text{Cat-N-SQ})(\text{Cat-N-BQ})$ .** Formulating a conclusive interpretation of the TRIR measurements for  $DQ_2$  requires that a distinction is made between the results obtained exciting at 525 and 1000 nm (Figure 8), and those resulting from excitation at 712 nm (Figure 9). In the first case, the transient spectra have strong similarities to those measured for **tpy** with 521 nm excitation. In particular, for both molecules, the most intense band centered at 1278  $\text{cm}^{-1}$  and its low frequency shoulder appear with a detectable delay after the excitation. The same is true for the absorption band at 1495  $\text{cm}^{-1}$ . However, there are also noticeable differences between the two samples: in  $DQ_2$ , the band at 1278  $\text{cm}^{-1}$  has a shoulder at higher frequency around 1300  $\text{cm}^{-1}$ , already evident at 1.8 ps delay. The shape of the 1495  $\text{cm}^{-1}$  band is definitely less asymmetric than that in the other sample, due to an additional bleaching at higher frequency. These discrepancies are due to the presence of two active ligands in the molecule, resulting in additional bands in those regions. The similarities observed for the two samples suggest that in both cases the  $hs\text{-Co}^{\text{II}}$  metastable electronic state is effectively populated. As in the case of **tpy**, the global analysis performed on the  $DQ_2$  data confirms this picture, and the resulting kinetic parameters are collected in Table 8. The values of  $\tau_1$  are very close to those in Table 7, as expected if the same dynamic process is involved. The average value of  $\tau_2$  ( $\sim 490$  ps) is in agreement with the results of Gentili et al.<sup>32</sup>

Table 7. Global Analysis Time ( $\tau_n$ ) and Kinetic ( $k_n$ ) Constants for the  $\text{Co}(\text{tpy})(\text{Cat-N-BQ})$  Complex

wavelength (nm)	$\tau_1$ (ps)	std. dev. (ps)	$k_1$ ( $\text{ps}^{-1}$ )	$\tau_2$ (ps)	std. dev. (ps)	$k_2$ ( $\text{ps}^{-1}$ )
$\lambda_0 = 490$	12.9	0.44	$7.73 \times 10^{-2}$	349.7	6.28	$2.86 \times 10^{-3}$
$\lambda_0 = 521$	14.2	0.67	$7.01 \times 10^{-2}$	359.6	7.44	$2.78 \times 10^{-3}$
$\lambda_0 = 1170$	7.43	0.87	$1.34 \times 10^{-1}$	348.7	10.30	$2.87 \times 10^{-3}$



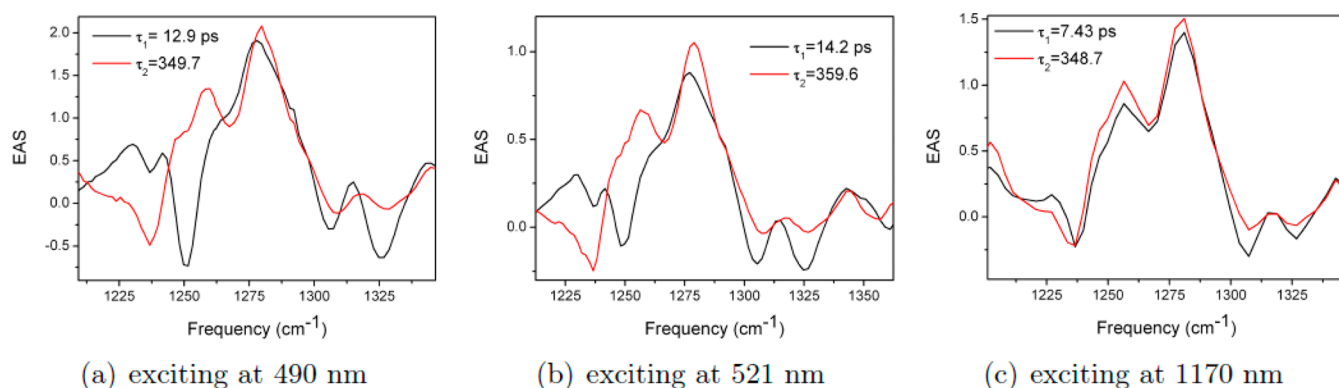


**Figure 10.** Calculated EAS of **tpy** in the 1220–1360  $\text{cm}^{-1}$  region: (a) excitation at 490 nm; (b) excitation at 521 nm; (c) excitation at 1170 nm. Time constants are taken from Table 7.

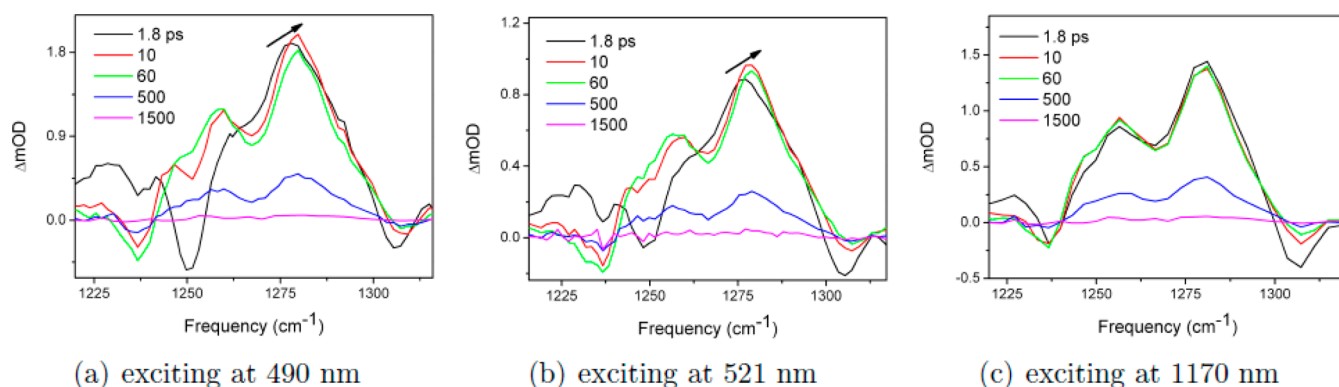


**Figure 11.** Absorption band detail from Figures 4 and 5, showing vibrational cooling dynamics: (a) excitation at 490 nm; (b) excitation at 521 nm; (c) excitation at 1170 nm.

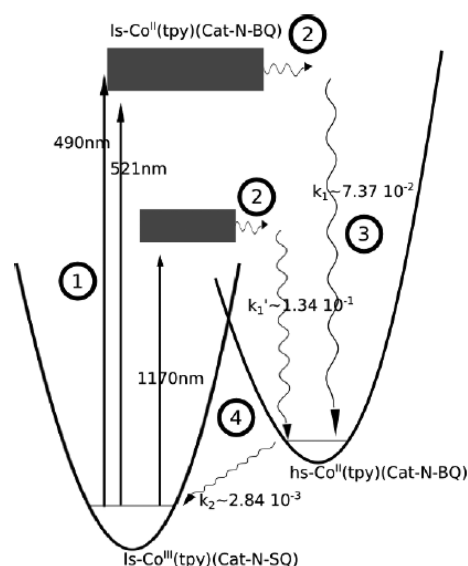


**Figure 12.** Schematic representation of potential energy surfaces for the **tpy** complex. Four steps are involved. 1 is the electronic excitation event: two different excited states are populated, depending on the pump pulse wavelength. 2 indicates ultrafast ISC processes leading to the same high-spin electronic state. 3 corresponds to vibrational cooling in the metastable state. 4 indicates the ground state recovery.

Then, for excitation at 525 and 1000 nm, the proposed excited state evolution involves the same four steps (Figure 13) discussed for **tpy**. When **DQ<sub>2</sub>** is excited at 712 nm, the TRIR

spectra are completely different. We already noticed that, in particular, the bands centered at 1278 and 1500  $\text{cm}^{-1}$  are absent. On the basis of our *ab initio* calculations, these bands are indicators of the *hs-Co<sup>II</sup>* metastable electronic state, and are the keys of our dynamical and spectral interpretation.

We can conclude that the excitation of **DQ<sub>2</sub>** at 712 nm does not induce any tautomeric transformation. Differently from the other cases, the transient IR spectrum of **DQ<sub>2</sub>** after excitation at 712 nm is largely dominated (Figure 9) by negative (bleaching) bands. The obvious interpretation is that in this case the very next step after the excitation does not involve any ISC process: the observed spectral evolution only concerns the ground state recovery. It is worth noticing that the excitation at 712 nm involves the **DQ<sub>2</sub>** absorption band attributed to the benzoquinonate ligand (see section 3.2); the fact that, on the contrary, excitation in the semiquinonate band ( $\lambda > 1000$  nm) invariably causes tautomeric interconversion both in **tpy** and **DQ<sub>2</sub>** suggests that in the two cases electronic excited states of substantially different nature are populated.

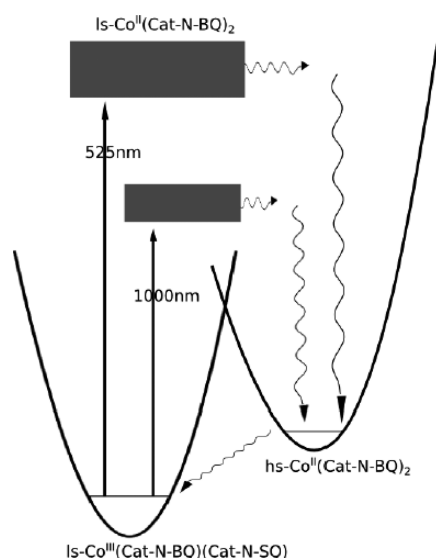
## 5. CONCLUSION

In this work, we investigated the valence tautomerism for two Co–dioxolene complexes ( $[\text{Co}(\text{tpy})(\text{Cat-N-SQ})]\text{PF}_6$  and  $\text{Co}(\text{Cat-N-BQ})(\text{Cat-N-SQ})$ ). Transient infrared spectroscopy, supported by DFT calculations, provides evidence that in both molecules optically induced VT takes place; it involves one-electron transfer from one dioxolene ligand to the  $e_g^*$  MOs, localized on the metal center. The ligand-to-metal charge transfer causes an increase of the distance between Co and ligands, and consequently a change of the ligand field acting on



Table 8. Global Analysis Time ( $\tau_n$ ) and Kinetic ( $k_n$ ) Constants for the Co(Cat-N-BQ)(Cat-N-SQ) Complex

wavelength (nm)	$\tau_1$ (ps)	std. dev. (ps)	$k_1$ ( $\text{ps}^{-1}$ )	$\tau_2$ (ps)	std. dev. (ps)	$k_2$ ( $\text{ps}^{-1}$ )
$\lambda_0 = 525$	14.3	0.62	$7.00 \times 10^{-2}$	448.1	10.8	$2.23 \times 10^{-3}$
$\lambda_0 = 1000$	12.5	0.54	$7.97 \times 10^{-2}$	451.2	12.6	$2.21 \times 10^{-3}$

Figure 13. Schematic representation of potential energy surfaces for  $\text{DQ}_2$ . The arrows represent the same four steps discussed for  $\text{tpy}$ .

the metal center. This triggers the spin transition from low-spin to high-spin configuration of the  $\text{Co}^{\text{II}}$ , thus modifying the magnetic properties of the molecules. Both  $\text{tpy}$  and  $\text{DQ}_2$  show the same behavior when excited around 520 nm (in the LMCT absorption band) and above 1000 nm, where the semiquinonate ligand absorbs: the transient IR spectra bring evidence, supported by the DFT calculations and in agreement with previous work<sup>40,50,65</sup> that the high-spin tautomeric state is populated via an ultrafast ISC process, followed by vibrational cooling (time constant  $\sim 7\text{--}14$  ps) in the potential well of the metastable hs state. The ground state recovery finally takes place with a much slower time constant ( $\sim 350$  ps for  $\text{tpy}$  and  $\sim 450$  ps for  $\text{DQ}_2$ ). In  $\text{DQ}_2$ , where two dioxolene ligands are present, excitation at  $\lambda = 712$  nm, corresponding to the absorption of the dioxolene in its benzoquinonate form, does not induce any tautomeric conversion. This evident wavelength selectivity of the photoconversion suggests that some specificity of the excited states involved in the process comes into play. In general, an ultrafast and highly efficient ligand-to-metal charge transfer via an optically excited state implies that both characters, metal and ligand, are part of the corresponding molecular orbital. While this picture is quite natural for excitation in the LMCT band, it is not obvious when the excitation takes place in absorption bands attributed to transitions of the active ligand(s). It is then plausible that the lack of tautomeric conversion upon excitation in the benzoquinonate absorption band of  $\text{DQ}_2$  reflects the much lower degree of metal character of the excited state molecular orbital, in comparison with the excited state involving the semiquinonate dioxolene moiety.

As a conclusion, the here reported data provide further insight of how it is possible to manipulate by laser pulses the magnetic properties of a suitable switchable molecular system. This is a particularly important point, since the control of the physical properties of these systems at molecular level is a basic

prerequisite for the design of memory devices. It should be emphasized that these properties in many known switchable materials are substantially different from those observed in the bulk. The possibility of exploiting the obtained results in more technologically suitable dilution states is under investigation.

## ■ ASSOCIATED CONTENT

### ● Supporting Information

A comparison between experimental data from literature and calculation results about the spin densities (Tables 1 and 3) and M–L distances (Tables 2 and 4) for the  $\text{DQ}_2$  complex in both of the electronic configurations ( $\text{ls-Co}^{\text{II}}$  and  $\text{hs-Co}^{\text{II}}$ ). This material is available free of charge via the Internet at <http://pubs.acs.org>.

## ■ AUTHOR INFORMATION

### Notes

The authors declare no competing financial interest.

## ■ ACKNOWLEDGMENTS

L. A. acknowledges the financial support of the Regione Toscana through the fund PORFSE 2007-2013 obiettivo 2 asse IV, project EPHODS. The authors acknowledge the support of the Italian 'Ministero dell'Istruzione dell'Università e della Ricerca' (FIRB 'Futuro in Ricerca' 2010, RBFR10Y5VW to M.D.D.). The financial support of the Cassa di Risparmio di Firenze is also gratefully acknowledged.

## ■ REFERENCES

- (1) Dei, A.; Gatteschi, D. Molecular (nano)Magnets as Test Grounds of Quantum Mechanics. *Angew. Chem. Int. Ed.* **2011**, *50*, 11852–11858.
- (2) Sanvito, S. Molecular Spintronics. *Chem. Soc. Rev.* **2011**, *40*, 3336–3355.
- (3) Zutic, I.; Fabian, J.; Das Sarma, S. Spintronics: Fundamentals and Applications. *Rev. Mod. Phys.* **2004**, *76*, 323–410.
- (4) Gajek, M.; Bibes, M.; Fusil, S.; Bouzehouane, K.; Fontcuberta, J.; Barthélémy, A.; Fert, A. Tunnel Junctions with Multiferroic Barriers. *Nat. Mater.* **2006**, *6*, 296–302.
- (5) Awschalom, D. D.; Flatté, M. E. Challenges for Semiconductor Spintronics. *Nat. Phys.* **2007**, *3*, 153–159.
- (6) Connolly, J. S.; Bolton, J. R. In *Photoinduced Electron Transfer*; Channon, M., Ed.; Elsevier: Amsterdam, The Netherlands, 1988.
- (7) Balzani, V.; Credi, A.; Scandola, F. *Supramolecular Photochemistry and Photophysics: Energy Conversion and Information-Processing Devices Based on Transition Metal Complexes*; NATO ASI Series; 1994; Vol. 448, pp 1–32.
- (8) Wishart, J. F.; Nocera, D. G., Eds. *Photochemistry and Radiation Chemistry: Complementary Methods for the Study of Electron Transfer*; ACS Advances in Chemistry Series 254; American Chemical Society: Washington, DC, 1988.
- (9) Hirjibehedin, C. F.; Lin, C.-Y.; Ternes, M.; P. Lutz, C. P.; Jones, B. A.; Heinrich, A. J. Large Magnetic Anisotropy of a Single Atomic Spin Embedded in a Surface Molecular Network. *Science* **2007**, *317*, 1199–1203.
- (10) Meier, F.; Zhou, L.; Wiebe, J.; Wiesendanger, R. Revealing Magnetic Interactions from Single-Atom Magnetization Curves. *Science* **2008**, *320*, 82–86.

- (11) Sato, O.; Tao, J.; Zhang, Y.-Z. Control of Magnetic Properties through External Stimuli. *Angew. Chem. Int. Ed.* **2007**, *46*, 2152–2187.
- (12) Sato, O.; Iyoda, T.; Fujishima, T.; Hashimoto, A.; Photoinduced, K. Magnetization of a Cobalt-Iron Cyanide. *Science* **1996**, *272*, 704–705.
- (13) Bleuzen, A.; Lomenech, C.; Escax, V.; Villain, F.; Varret, F.; Cartier dit Moulin, C.; Verdaguer, M. Photoinduced Ferrimagnetic Systems in Prussian Blue Analogues  $C'_xCo_4[Fe(CN)_6]_y$  ( $C'$ =Alkali Cation). 1. Conditions to Observe the Phenomenon. *J. Am. Chem. Soc.* **2000**, *122*, 6648–6652.
- (14) Dei, A. Photomagnetic Effects in Polycyanometallate Compounds: an Intriguing Future Chemically Based Technology? *Angew. Chem., Int. Ed.* **2005**, *44*, 1160–1163.
- (15) Gutlich, P.; Garcia, Y.; Theo, W. Photoswitchable Coordination Compounds. *Coord. Chem. Rev.* **2001**, *219–221*, 839–879.
- (16) Létard, J.-F.; Real, J. A.; Moliner, N.; Gaspar, A. B.; Capes, L.; Cador, O.; Kahn, O. Light Induced Excited Pair Spin State in an Iron(II) Binuclear Spin-Crossover Compound. *J. Am. Chem. Soc.* **1999**, *121*, 10630–10631.
- (17) Brady, C.; McGarvey, J. J.; McCusker, J. K.; Toftlund, H.; Hendrickson, D. N. Time-Resolved Relaxation Studies of Spin Crossover Systems in Solution. *Top. Curr. Chem.* **2004**, *235*, 1–22.
- (18) Hauser, A. Light-Induced Spin Crossover and the High-Spin  $\rightarrow$  Low-Spin Relaxation. *Top. Curr. Chem.* **2004**, *234*, 155–198.
- (19) Lapini, A.; Foggi, P.; Bussotti, L.; Righini, R.; Dei, A. Relaxation dynamics in three polypyridyl iron(II)-based complexes probed by nanosecond and sub-picosecond transient absorption spectroscopy. *Inorg. Chim. Acta.* **2008**, *361*, 3937–3943.
- (20) Sato, O.; Hayami, S.; Gu, Z.-Z.; Takahashi, K.; Nakajima, R.; Fujishima, A. Photo-Induced Reverse Valence Tautomerism in a Metastable Co Compound. *Chem. Phys. Lett.* **2002**, *355*, 169–174.
- (21) Carbonera, C.; Dei, A.; Sangregorio, C.; Létard, J.-F. Optically Switchable Behaviour of a Dioxolene Adduct of a Cobalt-Macrocyclic Complex. *Chem. Phys. Lett.* **2004**, *396*, 198–201.
- (22) Hendrickson, D. N.; Pierpont, C. G. Valence Tautomeric Transition Metal Complexes. *Top. Curr. Chem.* **2004**, *234*, 63–95.
- (23) Dei, A.; Gatteschi, D.; Sangregorio, C.; Sorace, L. Quinonoid Metal Complexes: Toward Molecular Switches. *Acc. Chem. Res.* **2004**, *37*, 827–835.
- (24) Carbonera, C.; Dei, A.; Létard, J.-F.; Sangregorio, C.; Sorace, L. Thermally and Light-Induced Valence Tautomeric Transition in a Dinuclear Cobalt–Tetraoxolene Complex. *Angew. Chem., Int. Ed.* **2004**, *43*, 3136–3138.
- (25) Evangelio, E.; Ruiz-Molina, D. Valence Tautomerism: New Challenges for Electroactive Ligands. *Eur. J. Inorg. Chem.* **2005**, *2005*, 2957–2971.
- (26) Sato, O.; Cui, A.; Matsuda, R.; Tao, J.; Hayami, S. Photo-Induced Valence Tautomerism in Co Complexes. *Acc. Chem. Res.* **2007**, *40*, 361–369.
- (27) Beni, A.; Carbonera, C.; Dei, A.; Létard, J. F.; Righini, R.; Sangregorio, C.; Sorace, L. Optically Induced Valence Tautomeric Interconversion in Cobalt Dioxolene Complexes. *J. Braz. Chem. Soc.* **2006**, *17*, 1522–1533.
- (28) Poneti, G.; Mannini, M.; Sorace, L.; Sainctavit, P.; Arrio, M.-A.; Otero, E.; Originski Cezar, J.; Dei, A. Soft-X-ray-Induced Redox Isomerism in a Cobalt Dioxolene Complex. *Angew. Chem., Int. Ed.* **2010**, *49*, 1954–1957.
- (29) Adams, D. M.; Li, B.; Simon, J. D.; Hendrickson, D. N. Photoinduced Valence Tautomerism in Cobalt Complexes Containing Semiquinone Anion as Ligand: Dynamics of the High-Spin  $[Co^{II}(3,5\text{-dtbsq})_2]$  to Low-Spin  $[Co^{III}(3,5\text{-dtbsq})(3,5\text{-dtbc})]$  Interconversion. *Angew. Chem., Int. Ed.* **1995**, *34*, 1481–1483.
- (30) Adams, D. M.; Hendrickson, D. N. Pulsed Laser Photolysis and Thermodynamics Studies of Intramolecular Electron Transfer in Valence Tautomeric Cobalt o-Quinone Complexes. *J. Am. Chem. Soc.* **1996**, *118*, 11515–11528.
- (31) Neuwahl, F.; Righini, R.; Dei, A. Femtosecond Spectroscopic Characterisation of the Two-Step Valence Tautomeric Interconversion Occurring in a Cobalt–Dioxolene Comple. *Chem. Phys. Lett.* **2002**, *352*, 408–414.
- (32) Gentili, P. L.; Bussotti, L.; Righini, R.; Beni, A.; Bogani, L.; Dei, A. Time-Resolved Spectroscopic Characterization of Photo-Induced Valence Tautomerism for a Cobalt–Dioxolene Complex. *Chem. Phys.* **2005**, *314*, 9–17.
- (33) Beni, A.; Dei, A.; Rizzitano, M.; Sorace, L. Unprecedented Optically Induced Long-Lived Intramolecular Electron Transfer in Cobalt–Dioxolene Complexes. *Chem. Commun.* **2007**, 2160–2162.
- (34) Beni, A.; Dei, A.; Laschi, S.; Rizzitano, M.; Sorace, L. Tuning the Charge Distribution and Photoswitchable Properties of Cobalt–Dioxolene Complexes by Using Molecular Techniques. *Chem.—Eur. J.* **2008**, *14*, 1804–1813.
- (35) Dapporto, P.; Dei, A.; Poneti, G.; Sorace, L. Complete Direct and Reverse Optically Induced Valence Tautomeric Interconversion in a Cobalt–Dioxolene Complex. *Chem.—Eur. J.* **2008**, *14*, 10915–10918.
- (36) Li, B.; Tao, J.; Sun, H.-L.; Sato, O.; Huang, R. B.; Zheng, L.-S. Side-Effect of Ancillary Ligand on Electron Transfer and Photo-dynamics of a Dinuclear Valence Tautomeric Complex. *Chem. Commun.* **2008**, 2269–2271.
- (37) Dei, A.; Poneti, G.; Sorace, L. Metal Dilution Effects on Entropy and Light-Induced Valence Tautomeric Interconversion in a 1:1 Cobalt–Dioxolene Complex. *Inorg. Chem.* **2010**, *49*, 3271–3277.
- (38) Schmidt, R. D.; Shultz, D. A.; Martin, J. D. Magnetic Bistability in a Cobalt bis(Dioxolene) Complex: Long-Lived Photoinduced Valence Tautomerism. *Inorg. Chem.* **2010**, *49*, 3162–3168.
- (39) Schmidt, R. D.; Shultz, D. A.; Martin, J. D.; Boyle, P. D. Goldilocks Effect in Magnetic Bistability: Remote Substituent Modulation and Lattice Control of Photo-Induced Valence Tautomerism and Light-Induced Thermal Hysteresis. *J. Am. Chem. Soc.* **2010**, *132*, 6261–6273.
- (40) Tourón Touceda, P.; Mosquera Vázquez, S.; Lima, M.; Lapini, A.; Foggi, P.; Dei, A.; Righini, R. Transient Infrared Spectroscopy: a New Approach to Investigate Valence Tautomerism. *Phys. Chem. Chem. Phys.* **2012**, *14*, 1038–1047.
- (41) Pierpont, C. G.; Buchanan, R. M. Transition Metal Complexes of o-Benzoquinone, o-Semiquinone, and Catecholate Ligands. *Coord. Chem. Rev.* **1981**, *38*, 45–87.
- (42) Pierpont, C. G.; Lange, C. W. The Chemistry of Transition Metal Complexes Containing Catechol and Semiquinone Ligands. *Prog. Inorg. Chem.* **1993**, *41*, 381–397.
- (43) Girgis, A. Y.; Balch, A. L. Catechol Oxidations. Characterization of Metal Complexes of 3,5-Di-tert-butyl-1,2-quinone 1-(2-Hydroxy-3,5-di-tert-butylphenyl)imine Formed by the Aerial Oxidation of 3,5-Di-tert-butylcatechol in the Presence of Ammonia and Divalent Metal Ions. *Inorg. Chem.* **1975**, *14*, 2724–2727.
- (44) Larsen, S.; Pierpont, C. G. Cobalt and Manganese Complexes of a Schiff Base Biquinone Radical Ligand. *J. Am. Chem. Soc.* **1988**, *110*, 1827–1832.
- (45) Simpson, C.; Boone, S.; Pierpont, C. Charge Distribution in Transition-Metal Complexes of a Schiff Base Biquinone Ligand. Structural and Electrochemical Properties of the  $M^{II}(\text{Cat-N-BQ})_2$ ,  $M^{III}(\text{Cat-N-BQ})(\text{Cat-N-SQ})$ ,  $M^{IV}(\text{Cat-N-SQ})_2$  Tautomeric Series. *Inorg. Chem.* **1989**, *28*, 4379–4385.
- (46) Chaudhuri, P.; Hess, M.; Hildenbrand, K.; Bill, E.; Weyhermüller, T.; Wieghardt, K. Ligand-Based Redox Isomers of  $[Zn(II)(C(28)H(40)NO(2))(2)]$ : Molecular and Electronic Structures of a Diamagnetic Green and a Paramagnetic Red Form. *Inorg. Chem.* **1999**, *38*, 2781–2790.
- (47) Bruni, S.; Caneschi, A.; Cariati, F.; Delfs, C.; Dei, A.; Gatteschi, D. Ferromagnetic Coupling between Semiquinone Type Tridentate Radical Ligands Mediated by Metal Ions. *J. Am. Chem. Soc.* **1994**, *116*, 1388–1394.
- (48) Evangelio, E.; Bonnet, M.-L.; Cabañas, M.; Nakano, M.; Sutter, J.-P.; Dei, A.; Robert, V.; Ruiz-Molina, D. Coexistence of Two Thermally Induced Intramolecular Electron Transfer Processes in a Series of Metal Complexes  $[M(\text{Cat-N-BQ})(\text{Cat-N-SQ})]/[M(\text{Cat-N-BQ})_2]$  ( $M=\text{Co}$ ,  $\text{Fe}$ , and  $\text{Ni}$ ) Bearing Non-Innocent Catechol-Based

Ligands: A Combined Experimental and Theoretical Study. *Chem.—Eur. J.* **2010**, *16*, 6666–6677.

(49) Caneschi, A.; Cornia, A.; Dei, A. Valence Tautomerism in a Cobalt Complex of a Schiff Base Diquinone Ligand. *Inorg. Chem.* **1998**, *37*, 3419–3421.

(50) Cador, O.; Dei, A.; Sangregorio, C.; Slagereen, J. V. Temperature-Induced Solid-State Valence Tautomeric Interconversion in Two Cobalt–Schiff Base Diquinone Complexes. *Inorg. Chem.* **2003**, *42*, 6432–6440.

(51) Tourón Touceda, P. Ph.D. Thesis, Atomic and Molecular Spectroscopy, Università degli Studi di Firenze, 2011.

(52) Azzaroli, N. Photoinduced Valence Tautomerism in Co Complexes: Vibrational Study by Transient Infrared Spectroscopy, Master Degree Thesis, Università degli Studi di Firenze, 2012.

(53) Khon, W.; Sham, L. J. Self-Consistent Equations Including Exchange and Correlation Effects. *Phys. Rev.* **1965**, *140*, A1133–A1138.

(54) Frisch, M. J.; Trucks, G. W.; Schlegel, H. B.; Scuseria, G. E.; Robb, M. A.; Cheeseman, J. R.; Scalmani, G.; Barone, V.; Mennucci, B.; Petersson, G. A.; et al. *Gaussian 09*, revision A.1; Gaussian, Inc.: Wallingford, CT, 2009.

(55) Lee, C.; Yang, W.; Parr, R. G. Development of the Colle-Salvetti Correlation-Energy Formula into a Functional of the Electron Density. *Phys. Rev. B* **1988**, *37*, 785–798.

(56) Caneschi, A.; Dei, A.; Gatteschi, D.; Tangoulis, V. Antiferromagnetic Coupling in a Six-Coordinate High Spin Cobalt(II)-Semiquinonato Complex. *Inorg. Chem.* **2002**, *41*, 3508–3512.

(57) van Stokkum, I. H. M.; Larsen, D. S.; van Grondelle, R. Global and Target Analysis of Time-Resolved Spectra. *Biochim. Biophys. Acta* **2004**, *1657*, 82–104.

(58) Hamm, P. Coherent Effects in Femtosecond Infrared Spectroscopy. *Chem. Phys.* **1995**, *200*, 415–429.

(59) Agrawal, G. P.; Baldeck, P. L.; Alfano, R. R. Temporal and Spectral Effects of Cross-Phase Modulation on Copropagating Ultrashort Pulses in Optical Fibers. *Phys. Rev. A* **1989**, *40*, 5063–5072.

(60) Wynne, K.; Hochstrasser, R. M. The Theory of Ultrafast Vibrational Spectroscopy. *Chem. Phys.* **1995**, *193*, 211–236.

(61) Sutherland, R. L. *Handbook of Nonlinear Optics*; Marcel Dekker Inc.: New York, 1996.

(62) Lapini, A.; Vázquez, S. M.; Touceda, P. T.; Lima, M. Cross-Phase Modulation in Visible-Pump/Mid-Infrared-Probe Spectroscopy. *J. Mol. Struct.* **2011**, *993*, 470–473.

(63) Henry, E. The Use of Matrix Methods in the Modeling of Spectroscopic Data Sets. *Biophys. J.* **1997**, *72*, 652–673.

(64) Satzger, H.; Zinth, W. Visualization of Transient Absorption Dynamics - Towards a Qualitative View of Complex Reaction Kinetics. *Chem. Phys.* **2003**, *295*, 287–295.

(65) Hamm, P.; Ohline, S.; Zinth, W. Vibrational Cooling after Ultrafast Photoisomerization of Azobenzene Measured by Femtosecond Infrared Spectroscopy. *J. Chem. Phys.* **1997**, *106*, 519–529.